ACS APPLIED ELECTRONIC MATERIALS

pubs.acs.org/acsaelm Article

Hydrogenation-Induced Phase Transition in Atomic-Layered α-$MoCl_3$ Driven by Laser Illumination in a Moist Atmosphere

Zhi Wang,[#] Yulan Han,[#] Jing Liang,[#] Haoliang Huang,[#] Chuansheng Hu, Ping Liu, Junxiang Xiang, Zeming Qi, Yalin Lu, Kaihui Liu,[*] Jun Jiang,[*] and Bin Xiang[*]

Cite This: *ACS Appl. Electron. Mater.* 2020, 2, 2678−2684 Read Online

ACCESS | Metrics & More | Article Recommendations | Supporting Information

ABSTRACT: Hydrogenation plays a critical role in tuning the material structural phase that fundamentally determines their electronic, optical, magnetic, and catalytic properties. However, prevailing hydrogenating techniques rely on noble-metal catalysis, high-temperature/pressure conditions, and high-energy proton implantation. Here, we report an optically controlled hydrogenation strategy of atomic-layered material α-$MoCl_3$ via laser illumination treatment in a moist atmosphere environment. With the assistant of laser, hydrogens are generated from the reaction between water molecules and highly electronegative element chlorine, intercalate into α-$MoCl_3$, and ultimately produce a more conductive phase with a maximum hydrogen-doping density of 0.04 wt %. Without laser, hydrogens are reversibly released and the structure restores to pristine α-$MoCl_3$. Density-functional theory studies reveal the facile mechanism of α-$MoCl_3$ hydrogenation including the dependence on the laser wavelength and power, the concomitant electronic phase transition, and improved material stability. Our results provide a plausible way for hydrogenating low-dimensional materials through precise control of laser treatment, which can find its multifunctional applications in hygrometer, photodetector, and photocontrollable smart devices.

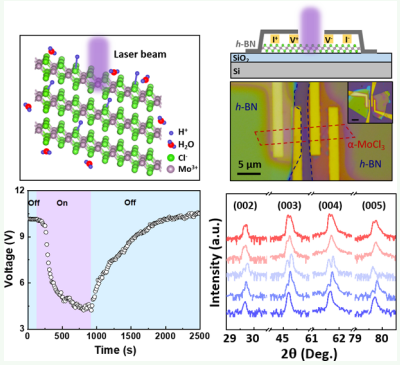

KEYWORDS: *atomic-layered α-$MoCl_3$, optically controlled hydrogenation, phase transition, moisture content, Density-functional theory (DFT)*

INTRODUCTION

Phase-change materials have attracted widespread attention due to diverse variations of physical and chemical properties during phase transitions such as metal−insulator transition (MIT) behavior,[1] optical emission,[2] the electrocaloric effect,[3] and hydrogen evolution catalysis,[4] especially yielding a relative change in electrical conductivity, which enriches more potential multifunctional applications.[5−7] Among a variety of approaches, hydrogenation is considered to be an effective way to tune material structural phase transition by modifying orbital occupancy,[1] band filling,[8] and polarization charge.[9,10] However, almost all current hydrogenation methods require noble-metal catalysis,[11,12] high-temperature and high-pressure conditions,[13−15] and high-energy proton implantation.[16,17] In addition, most conventional hydrogenating techniques are costly and lack in situ controllability. Therefore, the development of a more cost-effective and easily controlled hydrogenation strategy under mild reaction conditions is still challenging but highly desirable.

Layered α-$MoCl_3$, as a new typical transition metal trihalide (TMT), is highly stable in ambient air, insoluble in most common solvents (cold/hot water, ethanol, acetone, etc.), and has excellent thermal stability up to 580 K. Additionally, $MoCl_3$ is also predicted to be a narrow bandgap semiconductor.[18] Therefore, it is reasonable to expect that α-$MoCl_3$ should be a promising candidate for the construction of high-performance microelectronic devices in modern electronics and optoelectronics, while it has not been reported so far. Therefore, in this work, we report on the transport properties of intrinsic few-layered α-$MoCl_3$ devices and an optically controlled method to hydrogenate atomic-layered α-$MoCl_3$ material via laser illumination treatment in a moist atmosphere environment. With the assistance of laser illumination, highly electronegative element chlorine reacts with water molecules to generate hydrogen. Then, hydrogen intercalates layers of α-$MoCl_3$ and induces structural phase transition in α-$MoCl_3$. Noticeably, the phase transition driven by laser illumination exhibits high dependence on the excitation laser (both wavelength and power). In the meantime, the polarized electrons from intercalated hydrogens also have a modulation on the electronic structure of α-$MoCl_3$. Compared with the traditional hydrogenating methods, laser irradiation is much simpler, better controllable, and reliable in principle. Based on

Received: June 22, 2020
Accepted: July 13, 2020
Published: July 13, 2020

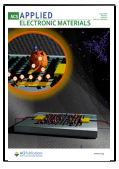

https://dx.doi.org/10.1021/acsaelm.0c00539
ACS Appl. Electron. Mater. 2020, 2, 2678−2684

the density-functional theory (DFT) calculations, we have revealed the hydrogenation mechanism and the concomitant improvement of electrical conductivity during hydrogenation.

RESULTS

Laser-Assisted Hydrogenation in Atomic-Layered α-$MoCl_3$. α-$MoCl_3$ was synthesized by a solid-state reaction method. Both the X-ray powder diffraction (XRD) pattern and the high-resolution transmission electron microscopy (HRTEM) image show that α-$MoCl_3$ has a cubic close-packed structure in which molybdenum has an [$MoCl_6$] octahedral coordination geometry (Section 1, Supporting Information). The lower structural symmetry of as-synthesized α-$MoCl_3$ originates from the formation of unique Mo−Mo chemical bonds with d^3-configuration,[19,20] which is distinguishable from other family members of two-dimensional (2D) transition metal trihalides (TMTs) such as $CrCl_3$,[21] $RhCl_3$,[21] and $RuCl_3$.[22,23] As a result, the [$MoCl_6$] octahedra becomes more distorted (compared to those in other TMTs, i.e., $CrCl_3$, α-$RuCl_3$) because of the formation of the Mo−Mo dimers in α-$MoCl_3$. Furthermore, one-third of the Cl atoms lying above the Mo−Mo bonds are shifted ∼0.28 Å above the layer. This increased freedom in α-$MoCl_3$ further enables larger distortions of [$MoCl_6$] octahedra and a more flexible host framework, which incidentally creates larger voids to accommodate the exotic atoms or molecules.[24] Therefore, an interesting metastable intercalative behavior, evoked from the reaction between polarized chlorine and hydrogen, can be more easily observed in the α-$MoCl_3$ structure. To address this issue, a laser was utilized to trigger the hydrogen intercalation process in the α-$MoCl_3$ (Figure 1a).

To investigate the electrical performance under laser illumination under a moist atmosphere, one typical four-probe nanodevice based on few-layer α-$MoCl_3$ (∼8 nm) is systematically studied in the following experiments (Section 2, Supporting Information). To weaken and suppress the interferential signals from the adjacent device channel as far as possible, we further opened a window to define the active region in the devices by transferring the thick h-BN flakes as protective encapsulation (Figure 1b). (Similar measurements were also carried out in the devices without h-BN encapsulation. Figure S5, Supporting Information.) Under an on/off (800/1600 s) pulse laser (410 nm, 9.6 mW·cm^{-2}) illumination, the time-dependent voltage shows a corresponding on/off response with a maximum ratio of 2.3 (Figure 1c) (We have further repeated the same transport measurements for more cycles, and the time-dependent voltage response demonstrates a periodic on/off switching behavior over multiple cycles, which means that the results are robust and convincing (Figure S6, Supporting Information).). Typically, Mo−Cl moieties in α-$MoCl_3$ are regarded as good hydrogen-bond acceptors forming a hydrogen-bonding Mo−Cl···H interaction.[25] Thus, such a photoelectric response is attributed to the laser-assisted reaction between chlorine and environmental moisture. As a result, the structure formation of H_xMoCl_3 occurs and charges are transferred between chlorine and hydrogen,[26] which finally enhances the electrical conductivity of α-$MoCl_3$. While after removing the laser, the intercalated hydrogens are gradually released due to the weakly bonded H···Cl in H_xMoCl_3, which reveals a reversible optical-controlled process of hydrogenation and dehydrogenation. We further investigated the mid- and far-infrared transmission spectroscopy of α-$MoCl_3$ before and after laser illumination.

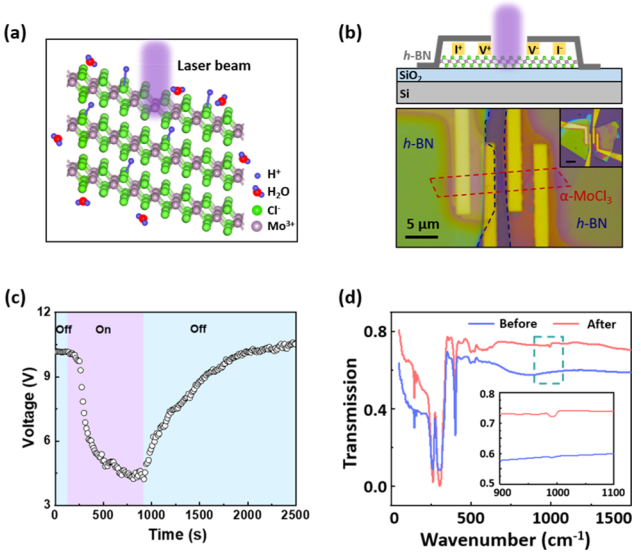

Figure 1. Laser-assisted hydrogenation in layered α-$MoCl_3$. (a) Schematic illustration of hydrogenation in the atomic-layered structure of α-$MoCl_3$ under laser illumination. (b) The top: the sketch of four-probe conductivity measurement of α-$MoCl_3$ under laser illumination. The bottom: the optical image of the multilayer α-$MoCl_3$-based device with h-BN as protective encapsulation, and the inset shows the optical image of the device at a lower magnification (scale bar: 10 μm). (c) Time-dependent voltage response in multilayer α-$MoCl_3$-based device under on-and-off laser illumination (410 nm, 9.6 mW·cm^{-2}) at a constant current flow of 1 nA. Illumination was on for 800 s and then off for 1600 s. (d) Mid- and far-infrared transmittance spectroscopy of α-$MoCl_3$ before and after laser illumination.

The characteristic peak at 994.1 cm^{-1}, corresponding to the weak H-bond vibration mode,[27] clearly demonstrates the formation of weakly bonded H···Cl during the hydrogen intercalation in the H_xMoCl_3 under laser illumination (Figure 1d).

To better understand the behavior of phase transition induced by hydrogenation in α-$MoCl_3$, we further investigate the structural evolution of α-$MoCl_3$ by XRD and selected area electron diffraction (SAED) as shown in Figure 2. Before laser illumination, there is only a single phase observed in α-$MoCl_3$, shown in XRD (Figure 2a) and SAED (Figure 2d). After laser illumination for 1.5 h, splitting behavior (Figure 2b) is observed in all of the XRD representative peaks of α-$MoCl_3$, indicating phase transformation. The splitting of the diffraction spots is also observed in SAED patterns (Figure 2e) after laser illumination, which is very similar to the reported results on lithium intercalation in lithium-ion batteries.[28,29] We deduce that the formation of H_xMoCl_3 during hydrogen intercalation leads to the coexisting phases of α-$MoCl_3$ and H_xMoCl_3 (The phases of α-$MoCl_3$ and H_xMoCl_3 possess one completely independent set of XRD diffraction patterns and SAED diffraction spots, respectively, which is generally regarded as pretty strong evidence for different structural phases.). The presence of hydrogen intercalated between the interlayers of α-$MoCl_3$ induces an in-plane tensor strain and out-of-plane compression strain.[30] Therefore, the lattice distance of H_xMoCl_3 along the c-axis is shorter than that of pristine α-$MoCl_3$, which explains why the locations of the XRD representative peaks of H_xMoCl_3 shift to higher θ angles compared to that of α-$MoCl_3$. In addition, H_xMoCl_3 is a

https://dx.doi.org/10.1021/acsaelm.0c00539
ACS Appl. Electron. Mater. 2020, 2, 2678−2684

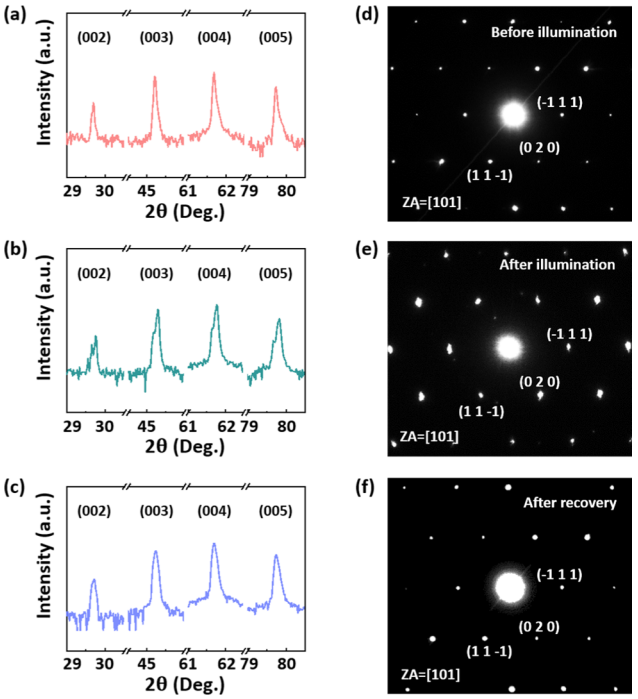

Figure 2. Structural evolution of α-$MoCl_3$ induced by hydrogenation. (a–c) Ex situ XRD characterization of α-$MoCl_3$ (a) before and (b) after laser illumination and (c) after recovery for 5 days, indicating reversible structure evolution. (d–f) Ex situ SAED characterization of α-$MoCl_3$ (d) before and (e) after laser illumination and (f) after recovery for 5 days. The samples illuminated by the laser were prepared in the same moisture of 90% utilized for the above characterization.

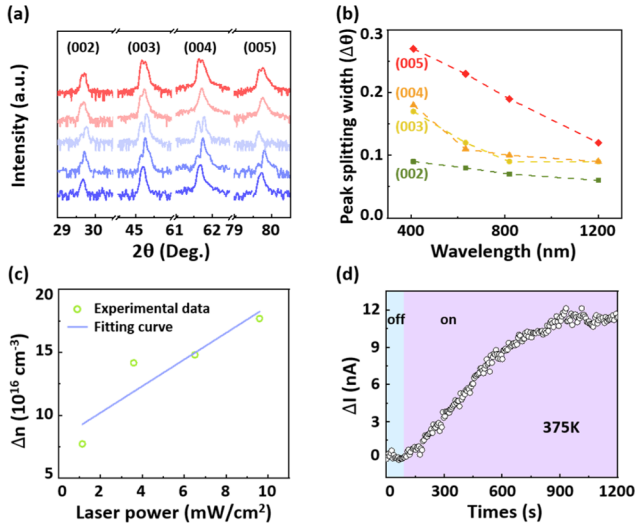

Figure 3. Determinant factors on the hydrogenation of α-$MoCl_3$. (a) Laser wavelength dependence of α-$MoCl_3$ XRD patterns at the same moisture content of 90%: before illumination (blue), 410 nm (light blue), 633 nm (gray blue), 820 nm (magenta), and 1200 nm (red). (b) Wavelength-dependent peak splitting width extracted from (a) XRD representative peaks of α-$MoCl_3$. (c) Laser power dependence of the hydrogen-intercalation-induced carrier concentration in α-$MoCl_3$ at a moisture content of 20%. The solid line is the fitting curve. (d) Current increment induced by hydrogenation in α-$MoCl_3$ still can be observed at 375 K under laser illumination (410 nm, 9.6 mW·cm^{-2}) with a moisture content of 90%, indicating excellent high-temperature resistance.

metastable phase, the intercalated hydrogen can reversibly be deintercalated from the host structure. After removing the laser illumination for 5 days, the structure is restored to pristine α-$MoCl_3$ with no splitting peak in XRD (Figure 2c) and no splitting spot in SAED (Figure 2f) patterns. Additionally, we also conducted the XRD characterization of α-$MoCl_3$ treated by laser illumination to probe the potential possibility of structural changes under a dry atmosphere. The result indicates that there are no structural changes for the illumination-treated sample under a dry atmosphere (Figure S7, Supporting Information), meaning that appropriate laser illumination and suitable moisture are a sufficient but not necessary condition for phase structure transition induced by hydrogenation in α-$MoCl_3$. Furthermore, according to the comparison results of XRD, SAED, and Raman spectroscopy (Figure S8, Supporting Information), the laser-assisted hydrogenation process in layered α-$MoCl_3$ is a reversible structure evolution and the structure can be restored intact to pristine α-$MoCl_3$, clearly demonstrating that there is no damage in the structure of α-$MoCl_3$ during the whole hydrogenation process.

Determinant Factors on Hydrogenation. Furthermore, we evaluate the effects of the laser wavelength, laser power, temperature, and ambient moisture on hydrogenation (Figure 3). Under fixed experimental conditions (laser power 20 mW·cm^2, temperature 300 K, and moisture content 90%), XRD peaks shift obviously and even split with an increasing laser wavelength (Figure 3a). In detail, the peak splitting width ($\Delta\theta$) decreases with an increasing laser wavelength (Figure 3b). We attribute the decrease to that lower photon energy (longer laser wavelength) illumination on the sample causes less chemical reaction for hydrogenation. Therefore, the higher the laser photon energy, the more the hydrogen intercalation reactions. As a result, more phase formation of H_xMoCl_3 leads to larger peak splitting. On the other hand, according to Bragg's law, it is well known that the derivative of sine function has a monotonically decreasing trend, which means that the increment of the dependent variable in sine function increases slower with the increase of the diffraction angle. Therefore, for the same increment (Δd) of lattice spacing, a high-angle peak shifts larger than a low-angle peak, and that is also why the splitting width of the higher-angle-peak exhibits higher sensitivity to laser wavelength variation under the same laser illumination. In addition to structural reorganization, the intercalation of hydrogen in α-$MoCl_3$ can also induce Mo 3d orbital-polarized electrons by means of substantial charges transferring from the hydrogen to the host material, causing electronic reorganization. Therefore, excess polarized electrons in α-$MoCl_3$ are generated due to charge transfer during hydrogen intercalation, which occupies the bottom of the conduction band and leads to electron doping in α-$MoCl_3$. These orbital-polarized electrons are delocalized in space and thus bestowing better conductivity on α-$MoCl_3$. Therefore, hydrogen intercalation could also be evaluated from the amount of excess polarized electrons (Δn) by measuring the conductance change of α-$MoCl_3$ devices. In this way, the effect of different moisture content on hydrogen intercalation (Section 3, Supporting Information) was also qualitatively studied, revealing that increasing the moisture content facilitates the hydrogen intercalation. Similarly, the linear relationship between Δn and laser power indicates that the amount of polarized electrons is proportional to the intensity of laser illumination (Figure 3c). Finally, we demonstrate that

https://dx.doi.org/10.1021/acsaelm.0c00539
ACS Appl. Electron. Mater. 2020, 2, 2678–2684

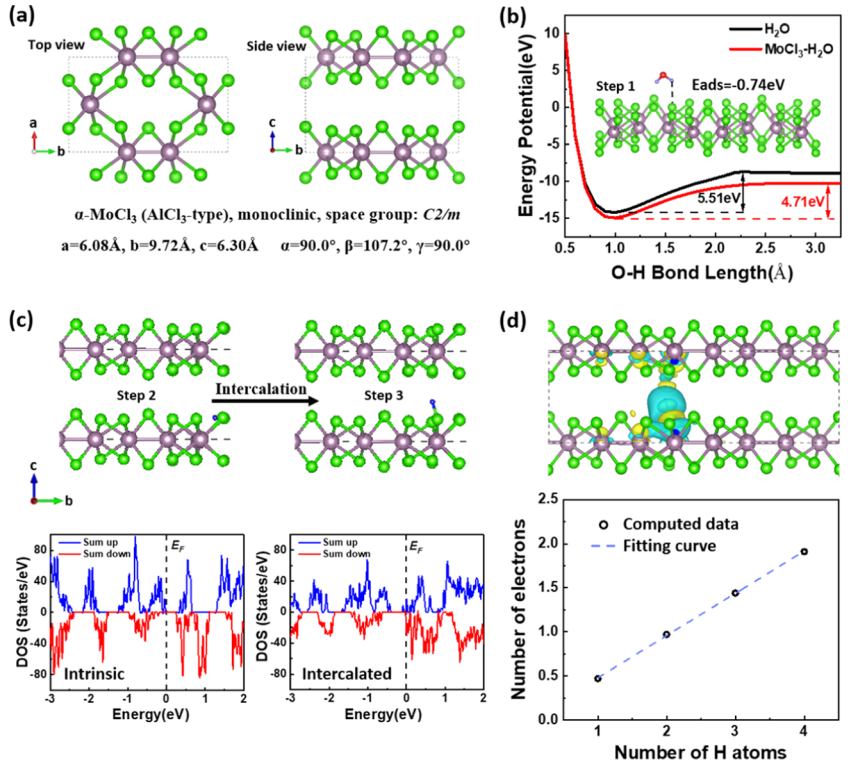

Figure 4. First-principles calculations for hydrogenation of α-$MoCl_3$. (a) Geometry optimization of the α-$MoCl_3$ crystal structure and the corresponding structural parameters in detail. (b) Variation of the energy potential of O−H bond breaking in water molecules and polar adsorption between the Cl and water molecules (inset). (c) Sketch map of the hydrogen intercalation in the α-$MoCl_3$ crystals (top panel) and the total density of states (DOS) of the α-$MoCl_3$ changes (bottom panel). (d) Hydrogenation-induced charge density difference plot (top panel) and the polarization charges contributed from hydrogenation (bottom panel).

hydrogenation in α-$MoCl_3$ has an excellent high-temperature resistance since the current increment can still be observed even at 375 K (Figure 3d).

Density-Functional Theory (DFT) Calculations. First-principles theory studies at the density-functional theory (DFT) level were applied to model the α-$MoCl_3$ structure, based on previously measured crystal parameters (Section 4, Supporting Information).[20] As shown in Figure 4a, the monoclinic structure of the α-$MoCl_3$ crystal belongs to the space group $C2/m$ and the computed lattice parameters of α-$MoCl_3$ are a = 6.08 Å, b = 9.72 Å, c = 6.30 Å, and β = 107.2°. Importantly, we confirmed the formation of the Mo−Mo bond along the b direction at a distance of 2.61 Å. Furthermore, the X-ray powder diffraction pattern of α-$MoCl_3$ predicted by our theoretical simulation is in good agreement with that obtained from the XRD experiment (Section 4, Supporting Information).

We further theoretically investigated the physical mechanism of dehydrogenation from water and hydrogen intercalation in α-$MoCl_3$ under the effect of laser illumination. In our calculations, we performed the effect of a laser equivalent to adding extra electrons into the α-$MoCl_3$ system.[31] As the extra electrons increase, the potential barrier of dehydrogenation from water decreases linearly, which means that sufficient laser energy and illumination time can provide enough extra electrons and decrease the potential barrier, thus helping the process of dehydrogenation from water (Figure S13, Supporting Information). There are three steps of the hydrogenation process in α-$MoCl_3$. Upon exposure of a moist atmosphere to the surface of α-$MoCl_3$, water molecules are activated by the surface Cl^- with an adsorption energy of −0.74 eV (inset of Figure 4b, step 1), resulting in the reduction of an energy barrier of O−H bond breaking by 0.8 eV. The subsequent hydrogen intercalation reaction is likely to proceed in the b direction of the α-$MoCl_3$ crystals, as shown in the top panel of Figure 4c. The effect of hydrogenation initially occurs on the surface of the structure (step 2), and then diffused along the b direction into the interior of the crystal (step 3). Hydrogen deintercalation of H_xMoCl_3 crystals is realized under ambient conditions after removing the laser illumination. Due to the metastability of hydrogen bonding Mo−Cl···H interaction in H_xMoCl_3 crystals, during a long time, the weakly bonded H···Cl tends to break and the intercalated hydrogen continuously pumps out spontaneously with the formation of a hydrogen or water molecule (a potential combination of the hydrogen and oxygen from the atmosphere) under natural conditions. Remarkably, the hydrogenation in α-$MoCl_3$ induces the transition from the semiconductor to the metallic phase, which were demonstrated by the total density of states (DOS) predicted by the Perdew−Burke−Ernzerhof (PBE) functional. Meanwhile, as shown in the bottom panel of Figure 4d, hydrogenation can effectively enhance the intrinsic poor electrical conductivity of α-$MoCl_3$ by providing free charge carriers at the bottom of the conduction band. To better describe the scarcity of hydrogen dopants estimated by the experiment, we adopted a 3 × 3 × 1 α-$MoCl_3$ supercell, in which the most stable adsorption position of hydrogen has an adsorption energy of −1.36 eV (Section 4, Supporting Information). This model was then used for studying the charge transfer between the hydrogen and the host material. The top panel of Figure 4d shows the side view of the hydrogen-induced charge density difference,

https://dx.doi.org/10.1021/acsaelm.0c00539
ACS Appl. Electron. Mater. 2020, 2, 2678−2684

indicating substantial charge transfer from the hydrogen to the host material during the intercalation process. The charge transfer between the intercalated hydrogen and the host was further confirmed by the Bader charge analysis developed by Henkelman et al.[32] As shown in the bottom panel of Figure 4d, the charge polarization induced by hydrogen intercalation is proportional to the number of hydrogen atoms. The induced charge per intercalated hydrogen atom is about 0.48 e^- (the slope of the fitting line), which can be interpreted as the equal number of free carriers in this system. These additional free carriers effectively improve the electrical conductivity in α-$MoCl_3$. Combined with the results of experiments and calculations, it leads us to one possible kinetic mechanism of phase change induced by hydrogen intercalation: hydrogen starts intercalating along the side of layered α-$MoCl_3$ by forming a hydrogen-bonding Mo−Cl···H interaction. Intercalated and unintercalated layers are formed during intercalation. This process can be manifested by the coexistence of the pristine α-$MoCl_3$ and the intercalate (H_xMoCl_3) in one crystal. Therefore, the hydrogen intercalation is in favor of the classical Rüdorff−Hofmann (RH) model. This mechanism of the hydrogenation-induced phase change is characterized by a sigmoid shape of the kinetic curve. As we know, the process of hydrogenation needs enough energy to surmount the potential barrier and form a metastable phase of H_xMoCl_3. The energy is supplied by laser illumination, i.e., the total photon energy (The total photon energy is proportional to laser frequency and power.). Thus, to put it in a nutshell, the total photon energy dependence of phase change kinetics has a sigmoidal shape as well.

DISCUSSION

An on/off switching behavior was demonstrated in a multilayer α-$MoCl_3$-based device under laser illumination in ambient moist air, a behavior ascribed to the effect of first-order phase transition from α-$MoCl_3$ to H_xMoCl_3. The rise and fall times were measured to be 800 and 1800 s, respectively, corresponding to the effect of reversible hydrogenation processes. These times reveal that on/off switching is not from a photoconductive effect. In general, the photoconductive effect is based on the generation of photoinduced carriers by laser illumination that can effectively improve the material conductivity. However, the relaxation and recombination times for photoinduced carriers are all in the ns to 10 s range, resulting in much shorter times for conductivity variation compared to our experimental results. To further study hydrogenation in the α-$MoCl_3$ layered structure, we provide a theoretical model of hydrogen intercalation based on the stability analysis of the α-$MoCl_3$ layered structure and predict the maximum amount of hydrogen intercalations in a 2 × 2 × 1 primitive unit cell. This calculated result reveals that our experimental value achieves only 0.04 wt % rather than the theoretical maximum capacity (0.5 wt %). One possible reason for this poor experimental hydrogenation performance is the limited laser energy absorption rate. Another reason could be the slow reaction rate of hydrogenation because of the limited capacity of hydrogen transport channels in the α-$MoCl_3$ layered structure.

CONCLUSIONS

In summary, this research demonstrates phase transition in 2D α-$MoCl_3$ induced by laser-assisted hydrogenation under a moist atmosphere. Our results reveal that hydrogen generation and hydrogen doping occur simultaneously in α-$MoCl_3$. Furthermore, it is found that a shorter laser wavelength (higher photon energy), a higher laser power, and higher ambient moisture could facilitate the hydrogenation. DFT calculations confirm the metastable structure formation of H_xMoCl_3 during the hydrogen intercalation. In addition, our results also suggest that hydrogenation is a promising method for tuning the electronic properties of materials. Taking advantage of the excellent controllability of laser illumination such as spatial resolution, photon energy, and illumination intensity, this work would open a new path for hydrogenating low-dimensional materials with a cost-effective and precisely controllable laser treatment toward multifunctional applications such as hygrometer, photodetector, and photocontrollable smart devices.

EXPERIMENTAL SECTION

Sample Preparation. Single-crystal α-$MoCl_3$ was prepared by a direct solid-state reaction method with mixtures of high-purity molybdenum pentachloride ($MoCl_5$, ≥99.6%, Aladdin) and molybdenum powders (Mo, ≥99.9%, Aladdin) at a molar ratio of $MoCl_5$/Mo = 1.8:1. This procedure must be performed under a moisture-free and oxygen-free atmosphere of prepurified nitrogen because of inducing readily deliquescence of $MoCl_5$ in moist air. The mixed powders were sealed into an evacuated quartz tube (ϕ12 mm × 10 cm, 10^{-2} Pa). The sealed ampoules were then placed into a muffle furnace and annealed for 10 h at 1073 K followed by furnace cooling. Notably, as the reaction mixtures can generate large quantities of gas at high-temperature, for security issues, the quartz tubes should be maintained by sufficient wall thickness (≥2 mm), as well as by slowly heating up. Subsequently, after being washed three times with ethanol, air- and thermal-stable, dark-red α-$MoCl_3$ single crystals can be obtained with a maximum dimension size of 15 mm × 8 mm × 0.2 mm.

Characterization. The as-prepared α-$MoCl_3$ single crystals were characterized by X-ray diffraction (XRD, Rigaku SmartLab, Cu Kα radiation), transmission electron microscopy (TEM, JEM-2010, JEOL), Raman spectroscopy (Renishaw Raman with a 532 nm laser), and X-ray photoelectron spectroscopy (XPS, ESCALab 250, Thermo-VG Scientific), respectively. The thickness of exfoliated α-$MoCl_3$ nanosheets was determined by atomic force microscopy (AFM, Bruker Dimension ICON, Billerica, MA) under ambient conditions. The room temperature mid- and far-infrared transmittance spectra of α-$MoCl_3$ were acquired on a Fourier transform infrared (FTIR) spectrometer (Bruker IFS 66v, Germany) on the infrared beamline station (U4) at the National Synchrotron Radiation Laboratory (NSRL, Hefei, China).

Device Fabrication. Few-layer α-$MoCl_3$ nanosheets were mechanically exfoliated onto the 285 nm SiO_2/Si substrates with prepatterned Cr/Au markers that are used for the subsequent fabrication alignment. We accomplished the set of contacts by the electron-beam lithography (EBL) technique. In these steps, briefly, the exfoliated nanosheets are spin-coated at 3000 rpm for 30 s with MMA (6% concentration in ethyl lactate), baked at 180 °C for 3 min, then spin-coated using the same parameters with PMMA (4% concentration in anisole), baked at 180 °C for 2 min, and subsequently exposed by electron-beam lithography. After development in IPA/H_2O = 7:3 solution for 30 s, reactive ion etching (RIE, Oxford, plasma Pro NGP 80) was used to remove organic pollutants deposited on the surface of α-$MoCl_3$ nanosheets, and then, we deposited metal contact materials (Ni/Au, 10:50 nm thickness) by magnetron sputtering and liftoff in acetone (40 min).

Measurements. The transport measurements were performed by a commercial semiconductor parameter analyzer (Keithley 4200SCS) equipped with the optical measurement system component. The devices mounted onto the printed circuit board (PCB) were then placed into an organic glass box (~30 cm × 20 cm × 20 cm). The

https://dx.doi.org/10.1021/acsaelm.0c00539
ACS Appl. Electron. Mater. 2020, 2, 2678−2684

illumination is directed through the reserved optical window in the box. The ambient moisture in the box was regulated by a small humidifier and monitored by a digital hygrometer in real time. We carried out several simulation experiments before the measurements to ensure that the whole test system was smooth and stable.

Calculations. The geometry optimizations of the periodic structures were performed using the projector augmented wave (PAW) method, implemented in the Vienna ab initio simulation package (VASP) code. We adopted a global hybrid generalized gradient approximation (GGA) functional to the exchange−correction functional and the Perdew−Burke−Ernzerhof (PBE) functional combined with van der Waals corrections (vdW-DFT). Based on the energy convergence tests, the cutoff energy is set to be 400 eV for all calculations. γ-centered k-point grids of $4 \times 2 \times 4$ for a α-$MoCl_3$ unit cell are chosen for relaxations and property calculations. Considering the low concentration of the intercalated hydrogen in real experiment, we built $2 \times 2 \times 1$ primitive unit cells to avoid the interactions between the periodic repeated hydrogens in the system. The positions of all ions and the unit cell parameters are relaxed for respective hydrogen concentrations to minimize the atomic forces with a force convergence of 0.01 eV·Å^{-1} and the total energy with an energy convergence of 10^{-4} eV.

■ ASSOCIATED CONTENT

Supporting Information

The Supporting Information is available free of charge at https://pubs.acs.org/doi/10.1021/acsaelm.0c00539.

Crystal structure of layered α-$MoCl_3$; AFM imaging of exfoliated α-$MoCl_3$ nanosheets; XPS and layer-dependent Raman spectroscopy of α-$MoCl_3$; calculated work function values; time-dependent voltage response and the stability for more cycles of the device without h-BN encapsulation; stability of a periodic on/off switching behavior over multiple cycles; XRD characterization of α-$MoCl_3$ illumination-treated under a dry atmosphere; Raman characterization of intrinsic α-$MoCl_3$ before hydrogenation and α-$MoCl_3$ after recovery from hydrogenation; the effect of different moisture contents on hydrogenation; identical structure of theory and experiment; stable adsorption position of hydrogen in α-$MoCl_3$; hydrogen adsorption energy with various intercalation concentrations; potential barrier of dehydrogenation from water under the effect of laser illumination (PDF)

■ AUTHOR INFORMATION

Corresponding Authors

Kaihui Liu − *State Key Laboratory for Mesoscopic Physics, School of Physics, Academy for Advanced Interdisciplinary Studies, Peking University, Beijing 100871, China;* orcid.org/0000-0002-8781-2495; Email: khliu@pku.edu.cn

Jun Jiang − *Hefei National Research Center for Physical Sciences at the Microscale and CAS Center for Excellence in Nanoscience, School of Chemistry and Materials Science, University of Science and Technology of China, Hefei, Anhui 230026, China;* orcid.org/0000-0002-6116-5605; Email: jiangj1@ustc.edu.cn

Bin Xiang − *Hefei National Research Center for Physical Sciences at the Microscale and Department of Materials Science & Engineering, CAS Key Lab of Materials for Energy Conversion, University of Science and Technology of China, Hefei, Anhui 230026, China;* Email: binxiang@ustc.edu.cn

Authors

Zhi Wang − *Hefei National Research Center for Physical Sciences at the Microscale and Department of Materials Science & Engineering, CAS Key Lab of Materials for Energy Conversion, University of Science and Technology of China, Hefei, Anhui 230026, China;* orcid.org/0000-0001-7972-6493

Yulan Han − *Hefei National Research Center for Physical Sciences at the Microscale and CAS Center for Excellence in Nanoscience, School of Chemistry and Materials Science, University of Science and Technology of China, Hefei, Anhui 230026, China*

Jing Liang − *State Key Laboratory for Mesoscopic Physics, School of Physics, Academy for Advanced Interdisciplinary Studies, Peking University, Beijing 100871, China;* orcid.org/0000-0001-6348-2068

Haoliang Huang − *National Synchrotron Radiation Laboratory, University of Science and Technology of China, Hefei 230029, China;* orcid.org/0000-0002-5686-5519

Chuansheng Hu − *National Synchrotron Radiation Laboratory, University of Science and Technology of China, Hefei 230029, China*

Ping Liu − *Hefei National Research Center for Physical Sciences at the Microscale and Department of Materials Science & Engineering, CAS Key Lab of Materials for Energy Conversion, University of Science and Technology of China, Hefei, Anhui 230026, China*

Junxiang Xiang − *Hefei National Research Center for Physical Sciences at the Microscale and Department of Materials Science & Engineering, CAS Key Lab of Materials for Energy Conversion, University of Science and Technology of China, Hefei, Anhui 230026, China*

Zeming Qi − *National Synchrotron Radiation Laboratory, University of Science and Technology of China, Hefei 230029, China*

Yalin Lu − *Hefei National Research Center for Physical Sciences at the Microscale and National Synchrotron Radiation Laboratory, University of Science and Technology of China, Hefei, Anhui 230026, China*

Complete contact information is available at: https://pubs.acs.org/10.1021/acsaelm.0c00539

Author Contributions

#Z.W., Y.H., J.L., and H.H. contributed to the work equally.

Notes

The authors declare no competing financial interest.

■ ACKNOWLEDGMENTS

B.X. gratefully acknowledges support from the National Key Research and Development Program of China (2017YFA0402902) and the Joint Fund of the National Natural Science Foundation Committee of China Academy of Engineering Physics (NSAF) (U1630108). K.L. is grateful for the support from the Bureau of Industry and Information Technology of Shenzhen (No. 201901161512) and the Key R&D Program of Guangdong Province (Grant No. 2019B010931001). This work was partially carried out at the USTC Centre for Micro and Nanoscale Research and Fabrication. Numerical calculations were done in the Supercomputing Center of University of Science and Technology of China.

https://dx.doi.org/10.1021/acsaelm.0c00539
ACS Appl. Electron. Mater. 2020, 2, 2678−2684

REFERENCES

(1) Chen, Y.; Wang, Z.; Chen, S.; Ren, H.; Wang, L.; Zhang, G.; Lu, Y.; Jiang, J.; Zhou, C.; Luo, Y. Non-catalytic hydrogenation of VO_2 in acid solution. *Nat. Commun.* **2018**, *9*, No. 818.

(2) Zhu, Y.; Chen, D.; Huang, L.; Liu, Y.; Brik, M. G.; Zhong, J.; Wang, J. Phase-transition-induced giant enhancement of red emission in Mn^{4+}-doped fluoride elpasolite phosphors. *J. Mater. Chem. C* **2018**, *6*, 3951−3960.

(3) Peng, B.; Zhang, Q.; Gang, B.; Leighton, G.; Shaw, C.; Milne, S. J.; Zou, B.; Sun, W.; Huang, H.; Wang, Z. Phase-transition induced giant negative electrocaloric effect in a lead-free relaxor ferroelectric thin film. *Energy Environ. Sci.* **2019**, *12*, 1708−1717.

(4) Zheng, Y. R.; Wu, P.; Gao, M. R.; Zhang, X. L.; Gao, F. Y.; Ju, H. X.; Wu, R.; Gao, Q.; You, R.; Huang, W. X.; Liu, S. J.; Hu, S. W.; Zhu, J.; Li, Z.; Yu, S. H. Doping-induced structural phase transition in cobalt diselenide enables enhanced hydrogen evolution catalysis. *Nat. Commun.* **2018**, *9*, No. 2533.

(5) Chen, S.; Wang, Z.; Ren, H.; Chen, Y.; Yan, W.; Wang, C.; Li, B.; Jiang, J.; Zhou, C. Gate-controlled VO_2 phase transition for high-performance smart windows. *Sci. Adv.* **2019**, *5*, No. eaav6815.

(6) Lu, H. Y.; Hao, L.; Wang, R.; Ting, C. S. Ferromagnetism and superconductivity with possible p+ ip pairing symmetry in partially hydrogenated graphene. *Phys. Rev. B* **2016**, *93*, No. 241410.

(7) Xu, D. D.; Deng, X.; Zhao, Y. F.; Ma, R. R.; Zhong, N.; Huang, R.; Peng, H.; Xiang, P. H.; Duan, C. G. Hydrogenation dynamics of electrically controlled metal-insulator transition in proton-gated transparent and flexible WO_3 transistors. *Adv. Funct. Mater.* **2019**, *29*, No. 1902497.

(8) Yoon, H.; Choi, M.; Lim, T. W.; Kwon, H.; Ihm, K.; Kim, J. K.; Choi, S. Y.; Son, J. Reversible phase modulation and hydrogen storage in multivalent VO_2 epitaxial thin films. *Nat. Mater.* **2016**, *15*, 1113−1119.

(9) Chen, S.; Wang, Z.; Fan, L.; Chen, Y.; Ren, H.; Ji, H.; Natelson, D.; Huang, Y.; Jiang, J.; Zou, C. Sequential insulator-metal-insulator phase transitions of VO_2 triggered by hydrogen doping. *Phys. Rev. B* **2017**, *96*, No. 125130.

(10) Wang, X.; Zhang, G.; Wang, Z.; Yang, L.; Li, X.; Jiang, J.; Luo, Y. Metal-enhanced hydrogenation of graphene with atomic pattern. *Carbon* **2019**, *143*, 700−705.

(11) Ai, Y.; Hu, Z.; Liu, L.; Zhou, J.; Long, Y.; Li, J.; Ding, M.; Sun, H. B.; Liang, Q. Magnetically hollow Pt nanocages with ultrathin walls as a highly integrated nanoreactor for catalytic transfer hydrogenation reaction. *Adv. Sci.* **2019**, *6*, No. 1802132.

(12) Lin, L.; Yao, S.; Gao, R.; Liang, X.; Yu, Q.; Deng, Y.; Liu, J.; Peng, M.; Jiang, Z.; Li, S.; Li, Y. W.; et al. A highly CO-tolerant atomically dispersed Pt catalyst for chemoselective hydrogenation. *Nat. Nanotechnol.* **2019**, *14*, 354−361.

(13) Selcuk, S.; Zhao, X.; Selloni, A. Structural evolution of titanium dioxide during reduction in high-pressure hydrogen. *Nat. Mater.* **2018**, *17*, 923−928.

(14) Smith, D.; Howie, R. T.; Crowe, I. F.; Simionescu, C. L.; Muryn, C.; Vishnyakov, V.; Novoselov, K. S.; Kim, Y. J.; Halsall, M. P.; Gregoryanz, E.; Proctor, J. E. Hydrogenation of graphene by reaction at high pressure and high temperature. *ACS Nano* **2015**, *9*, 8279−8283.

(15) Chen, X.; Liu, L.; Peter, Y. Y.; Mao, S. S. Increasing solar absorption for photocatalysis with black hydrogenated titanium dioxide nanocrystals. *Science* **2011**, *331*, 746−750.

(16) Liu, N.; Häublein, V.; Zhou, X.; Venkatesan, U.; Hartmann, M.; Mačković, M.; Nakajima, T.; Spiecker, E.; Osvet, A.; Frey, L.; Schmuki, P. "Black" TiO_2 nanotubes formed by high-energy proton implantation show noble-metal-*co*-catalyst free photocatalytic H_2-evolution. *Nano Lett.* **2015**, *15*, 6815−6820.

(17) Shi, J.; Zhou, Y.; Ramanathan, S. Colossal resistance switching and band gap modulation in a perovskite nickelate by electron doping. *Nat. Commun.* **2014**, *5*, No. 4860.

(18) Miró, P.; Audiffred, M.; Heine, T. An atlas of two-dimensional materials. *Chem. Soc. Rev.* **2014**, *43*, 6537−6554.

(19) Hillebrecht, H.; Schmidt, P. J.; Rotter, H. W.; Thiele, G.; Zönnchen, P.; Bengel, H.; Cantow, H.-J.; Magonov, S. N.; Whangbo, M.-H. Structural and scanning microscopy studies of layered compounds MCl_3 (M = Mo, Ru, Cr) and $MOCl_2$ (M = V, Nb, Mo, Ru, Os). *J. Alloys Compd.* **1997**, *246*, 70−79.

(20) McGuire, M. A.; Yan, J.; Lampen-Kelley, P.; May, A. F.; Cooper, V. R.; Lindsay, L.; Puretzky, A.; Liang, L.; KC, S.; Cakmak, E.; Calder, S.; Sales, B. C. High-temperature magnetostructural transition in van der Waals-layered α-$MoCl_3$. *Phys. Rev. Mater.* **2017**, *1*, No. 064001.

(21) McGuire, M. A. Crystal and magnetic structures in layered, transition metal dihalides and trihalides. *Crystals* **2017**, *7*, No. 121.

(22) Cantow, H. J.; Hillebrecht, H.; Magonov, S. N.; Rotter, H. W.; Drechsler, D.-P. M.; Thiele, G. Atomic structure and superstructure of α-$RuCl_3$ by scanning tunneling microscopy. *Angew. Chem., Int. Ed.* **1990**, *29*, 537−541.

(23) Johnson, R. D.; Williams, S. C.; Haghighirad, A. A.; Singleton, J.; Zapf, V.; Manuel, P.; Mazin, I. I.; Li, Y.; Jeschke, H. O.; Valentí, R.; Coldea, R. Monoclinic crystal structure of α-$RuCl_3$ and the zigzag antiferromagnetic ground state. *Phys. Rev. B* **2015**, *92*, No. 235119.

(24) Zhang, J.; Li, H.; Liao, C. Z.; Lau, V. W. H.; Wong, K. W.; Chang, C. K.; Sheu, H.-S.; Shih, K.; Kang, Y. M. New Barium Vanadate $Ba_xV_2O_5$ ($x\approx0.16$) for Fast Lithium Intercalation: Lower Symmetry for Higher Flexibility and Electrochemical Durability. *Small Methods* **2020**, *4*, No. 1900585.

(25) Aullón, G.; Bellamy, D.; Orpen, A. G.; Brammer, L.; Bruton, E. A. Metal-bound chlorine often accepts hydrogen bonds. *Chem. Commun.* **1998**, 653−654.

(26) Lin, C.; Zhu, X.; Feng, J.; Wu, C.; Hu, S.; Peng, J.; Guo, Y.; Peng, L.; Zhao, J.; Huang, J.; Yang, J.; Xie, Y. Hydrogen-incorporated TiS_2 ultrathin nanosheets with ultrahigh conductivity for stamp-transferrable electrodes. *J. Am. Chem. Soc.* **2013**, *135*, 5144−5151.

(27) Deka, P.; Hazarika, A.; Deka, R. C.; Bharali, P. Influence of CuO morphology on the enhanced catalytic degradation of methylene blue and methyl orange. *RSC Adv.* **2016**, *6*, 95292−95305.

(28) Chrissafis, K.; Zamani, M.; Kambas, K.; Stoemenos, J.; Economou, N. A.; Samaras, I.; Julien, C. Structural studies of MoS_2 intercalated by lithium. *Mater. Sci. Eng. B* **1989**, *3*, 145−151.

(29) Ramana, C. V.; Mauger, A.; Gendron, F.; Julien, C. M.; Zaghib, K. Study of the Li-insertion/extraction process in $LiFePO_4/FePO_4$. *J. Power Sources* **2009**, *187*, 555−564.

(30) Yang, L.; Cui, X.; Zhang, J.; Wang, K.; Shen, M.; Zeng, S.; Dayeh, S. A.; Feng, L.; Xiang, B. Lattice strain effects on the optical properties of MoS_2 nanosheets. *Sci. Rep.* **2014**, *4*, No. 5649.

(31) Yang, L.; Li, X.; Zhang, G.; Cui, P.; Wang, X.; Jiang, X.; Zhao, J.; Luo, Y.; Jiang, J. Combining photocatalytic hydrogen generation and capsule storage in graphene based sandwich structures. *Nat. Commun.* **2017**, *8*, No. 16049.

(32) Tang, W.; Sanville, E.; Henkelman, G. A grid-based Bader analysis algorithm without lattice bias. *J. Phys.: Condens. Matter* **2009**, *21*, No. 084204.

https://dx.doi.org/10.1021/acsaelm.0c00539
ACS Appl. Electron. Mater. 2020, 2, 2678−2684